PAPER • OPEN ACCESS

Investigating pump harmonics generation in a SNAIL-based traveling wave parametric amplifier

View the article online for updates and enhancements.

Investigating pump harmonics generation in a SNAIL-based traveling wave parametric amplifier

A Yu Levochkina[1,2] , **H G Ahmad**[1,2] , **P Mastrovito**[1,2], **I Chatterjee**[1,2] , **G Serpico**[1],
L Di Palma[1] , **R Ferroiuolo**[1] , **R Satariano**[2], **P Darvehi**[2] , **A Ranadive**[3], **G Cappelli**[3],
G Le Gal[3] , **L Planat**[4], **D Montemurro**[1,2] , **D Massarotti**[2,5], **F Tafuri**[1,6] , **N Roch**[3],
G P Pepe[1,2] **and M Esposito**[2,*]

[1] Department of Physics, University Federico II, Naples 80126, Italy
[2] CNR-SPIN, Complesso di Monte S. Angelo, via Cintia, Napoli 80126, Italy
[3] Université Grenoble Alpes, CNRS, Grenoble INP, Institut Néel, 38000 Grenoble, France
[4] Silent Waves, Grenoble, France
[5] Department of Electrical Engineering and Information Technology, University Federico II, Naples 80125, Italy
[6] CNR INO, Largo Enrico Fermi 6, Florence 50125, Italy

E-mail: martina.esposito@spin.cnr.it

CrossMark

Abstract

Traveling wave parametric amplifiers (TWPAs) are extensively employed in experiments involving weak microwave signals for their highly desirable quantum-limited and broadband characteristics. However, TWPAs' broadband nature comes with the disadvantage of admitting the activation of spurious nonlinear processes, such as harmonics generation, that can potentially degrade amplification performance. Here we experimentally investigate a Josephson TWPA device with superconducting nonlinear asymmetric inductive element-based unit cells focusing on the amplification behaviour along with the generation of second and third harmonics of the pump. By comparing experimental results with transient numerical simulations, we demonstrate the influence of Josephson junctions' fabrication imperfections on the occurrence of harmonics and on the gain behaviour.

Keywords: superconducting quantum devices, Josephson metamaterials,
Traveling Wave Parametric Amplifiers

1. Introduction

A Josephson traveling wave parametric amplifier (JTWPA) is in essence a nonlinear superconducting transmission line constituted of an array of Josephson junctions-based unit cells. In virtue of its quantum-limited noise property and wide bandwidth operation, such device is a highly valuable tool for microwave signal amplification [1–12] and entanglement generation [13–16]. Amplification in JTWPAs occurs through a nonlinear wave-mixing process; when an intense pump at frequency f_p and a weak signal at frequency f_s are applied at the input of the device, the pump periodically modulates the nonlinear inductance of the Josephson junctions leading to an energy transfer from the pump itself to the signal mode and to an idler mode, at frequency f_i. Depending on the order of the nonlinearity, three wave-mixing ($f_p = f_s + f_i$) and four wave-mixing ($2f_p = f_s + f_i$) amplification processes can be distinguished [17–19]. Due

---
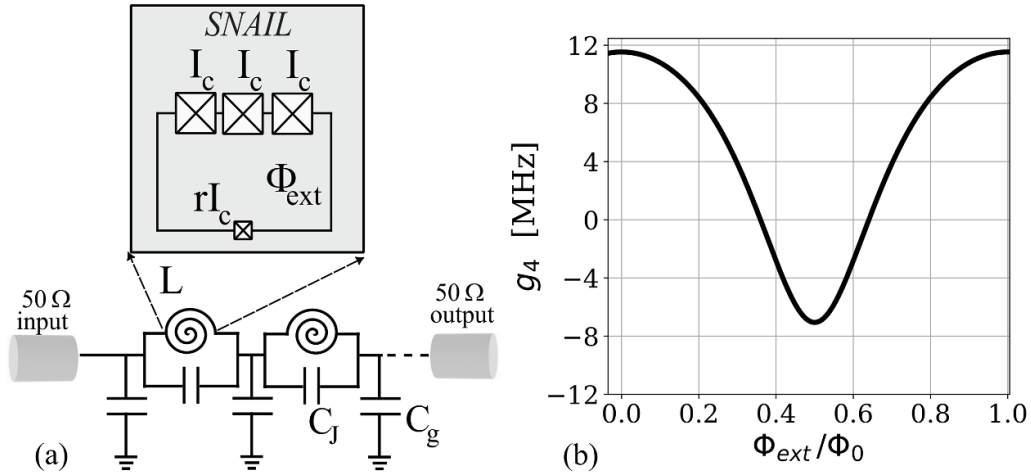
Figure 1. (a) Sketch of the *Reversed Kerr TWPA* device under investigation. C_g indicates the unit cell capacitance to ground, C_J the unit cell Josephson capacitance and L the inductance per unit cell. The SNAIL symbols are shown with opposite orientation for adjacent cells indicating the alternating flux polarity design. The inset is a sketch of the SNAIL element which includes three large JJs with critical current I_c and one small JJ with critical current rI_c. The main device's parameters and the methods for their estimation are reported in appendix. (b) 4WM nonlinear coefficient g_4 as a function of applied magnetic flux for the device under study.

to the large TWPA bandwidth, energy from the pump can also leak creating undesired additional modes that still satisfy energy conservation, such as sidebands (combinations of pump and signal/idler tones) [8, 20–23] and pump harmonics [24–26]. The dominant spurious tones are the second and the third harmonics of the pump, which in turn depend on the nonlinear coefficients associated with three wave-mixing (3WM) and four wave-mixing (4WM) interactions respectively.

In this article, we explore the behaviour of pump harmonics arising in JTWPAs, focusing on a *Reversed Kerr TWPA* [7] device, characterized by a superconducting nonlinear asymmetric inductive element (SNAIL)-based unit cell [27]. A key advantage of adopting a SNAIL-based JTWPA is the possibility to control both 3WM and 4WM nonlinear coefficients by an external magnetic flux [7, 12, 28], making it an ideal testing device for investigating spurious modes. In the specific case of a *Reversed Kerr TWPA*, 3WM nonlinear processes are inhibited by deliberately designing the unit cells with alternating flux polarity (since the 3WM nonlinear coefficient is an odd function of the flux) [7]. In such a way, in an ideal device, the second harmonic generation (SHG) of the pump, at frequency $f_{SH} = 2f_p$, should be in principle negligible at any flux value, while the third harmonic generation (THG), at frequency $f_{TH} = 3f_p$, is expected to be dominant and flux dependent.

We present an experimental study of gain, second, and third harmonics generation as a function of magnetic flux and pump amplitude. In contrast to ideal predictions, we observe a non-negligible presence of pump SHG. By means of numerical simulations, performed with *WRspice* [29] software, we can reproduce the experimental behaviour when a spread in the critical current of the Josephson junctions (JJs) is taken into account.

Understanding the effects of fabrication tolerance on JTWPAs' performance is an open challenge and has recently been a topic of in-depth numerical investigations [30, 31]. Our detailed study of nonlinear processes in the presence of JJs fabrication imperfections contributes to explaining the origin of unexpected harmonics in JTWPAs, providing new experimental insights supported by robust numerical models.

2. Device description

The *Reversed Kerr TWPA* under investigation is nominally identical to the one reported in [7] and it is sketched in figure 1(a). In the figure, I_C indicates the critical current, C_g indicates the unit cell capacitance to ground, C_J the unit cell Josephson capacitance and L the inductance per unit cell. Additional details on circuit parameters are reported in appendix. A key design aspect for this device is that SNAILs are oriented in such a way that the external magnetic flux has opposite sign for adjacent unit cells (alternating flux polarity), aiming at the suppression of the overall 3WM nonlinearity [32] and therefore of SHG. By assuming negligible 3WM nonlinear processes, the wave equation describing the propagation through the device can be written as

$$\frac{\partial^2 \phi}{\partial x^2} - \frac{1}{\omega_0^2} \frac{\partial^2 \phi}{\partial t^2} + \frac{1}{\omega_J^2} \frac{\partial^4 \phi}{\partial x^2 \partial t^2} - 8g_4 \frac{R_Q}{\pi \omega_0 Z} \frac{\partial}{\partial x}\left[\left(\frac{\partial \phi}{\partial x}\right)^3\right] = 0,$$
(1)

where $\omega_J = \sqrt{1/(LC_J)}$ and $\omega_0 = \sqrt{1/(LC_g)}$ are the plasma frequency and the characteristic frequency of the transmission line, $R_Q = h/(4e^2)$, $Z = \sqrt{L/C_g}$ is the characteristic impedance of the transmission line and g_4 is the flux-dependent 4WM nonlinear coefficient [7] indicating the rate
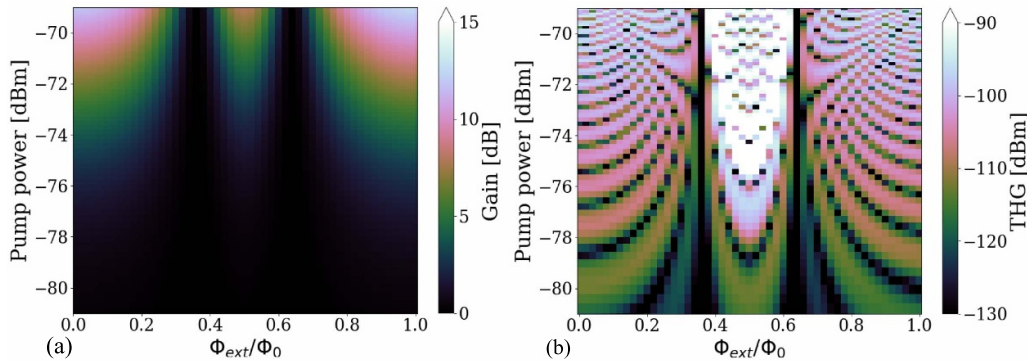
Figure 2. Couple mode equation (CME) theory predictions for gain (a) and THG of the pump (b) as a function of pump power and external magnetic flux. Pump frequency $f_p = 4\,\text{GHz}$, signal frequency $f_s = 3.9\,\text{GHz}$. The signal power is assumed to be lower than 1 dB compression point power of the device. The plots have been obtained with the open source software tool CMETANA (Couple Mode Equation Theory Analyzer) [35] which provides a user-friendly environment for CME predictions of JTWPAs starting from unit cells parameters. The exact analytical expressions are reported in appendix and in CMETANA's documentation.

at which the 4WM nonlinear processes occur. The dependence of g_4 on the external magnetic flux is reported in figure 1(b), while the full analytical expression is reported in appendix.

Following the standard approach developed in [24, 33] for JTWPAs and subsequently generalized to the case of SNAIL-based unit cells [2], we can use the standard couple mode equation (CME) theory to calculate the expected 4WM gain and the amplitude of the THG of the pump. Specifically, when 4WM gain is calculated, pump, signal and idler modes are included in the wave equation ansatz while, for the THG case, only the pump and its third harmonic are considered. The analytically calculated CME predictions are reported in figure 2 as a function of pump power and external magnetic flux. In order to accommodate all the relevant modes within the typical 4–12 GHz experimental frequency region of circuit-QED [34], we set the pump frequency $f_p = 4\,\text{GHz}$ and the signal frequency $f_s = 3.9\,\text{GHz}$. The exact analytical expressions are reported in appendix.

Being both 4WM processes, the gain and THG display the same flux-dependent behaviour associated with the typical 4WM g_4 nonlinear coefficient (figure 1(b)). Analytical CME predictions provide a useful benchmark when a new device is experimentally tested for the first time. Nevertheless, as reported in the following section, this simplified theoretical approach is not suitable to describe the full broadband experimental behaviour due to the constraint of including only a limited number of propagating tones.

3. Experimental results

The device has been experimentally measured at a temperature of 10 mK in a dilution refrigerator with a standard microwave experimental setup (see appendix). In figure 3(a), we report the device transmission (S_{21} parameter) measured with a vector network analyzer (VNA) with and without the presence of the pump tone at frequency $f_p = 4\,\text{GHz}$, when external magnetic

flux Φ_{ext}/Φ_0 is equal to 0.5. We deliberately chose the VNA settings in order to be able to detect the pump. When the pump is on, we observe 4WM gain along with the generation of the pump's harmonics. The VNA plots have an illustrative purpose, providing an example of the frequency-dependent behaviour of the device when pumped. To accurately investigate the generation of 4WM gain in the presence of pump harmonics, we perform a detailed spectral power characterization of the relevant frequency tones using a spectrum analyzer (SA). We set the pump frequency $f_p = 4\,\text{GHz}$ and we measure the intensity of a signal tone, at frequency $f_s = 3.9\,\text{GHz}$, as a function of the external magnetic flux and pump power (figure 3(b)). In the same conditions, we also measure the SHG, at frequency $f_{\text{SH}} = 8\,\text{GHz}$, and the THG of the pump, at frequency $f_{\text{TH}} = 12\,\text{GHz}$. The measured power is calibrated at the output of the device. The signal power at device input is $P_s = -110\,\text{dBm}$. The experimental results of harmonics measurements are reported in figure 4 [36].

We observe 4WM gain (figure 3(b)) and THG (figure 4(b)) which periodically change with the applied magnetic flux, following the behaviour of the SNAIL 4WM nonlinear coefficient, as qualitatively expected from CME theory (figure 1(b)). In contrast with what is ideally predicted for a SNAIL JTWPA with alternated flux polarity structure, we observe a non-negligible flux depended SHG power spectral density which for some flux and pump power values is comparable or larger than the THG one. We stress that for an accurate quantitative comparison between the measured spectral power of SHG and THG one should also consider that losses in the device under study increase for larger frequencies, specifically they approximately increase of 1 dB per GHz [7]. In addition, when the pump input power at the device exceeds roughly $-71\,\text{dBm}$, we measure a sudden drop in the device's experimental transmission due to the saturation of the JJ critical current which is not described by CME theory.

Finally, we also verify that the presence of the signal tone at the JTWPA input does not significantly influence the pump's harmonics generation (see appendix).
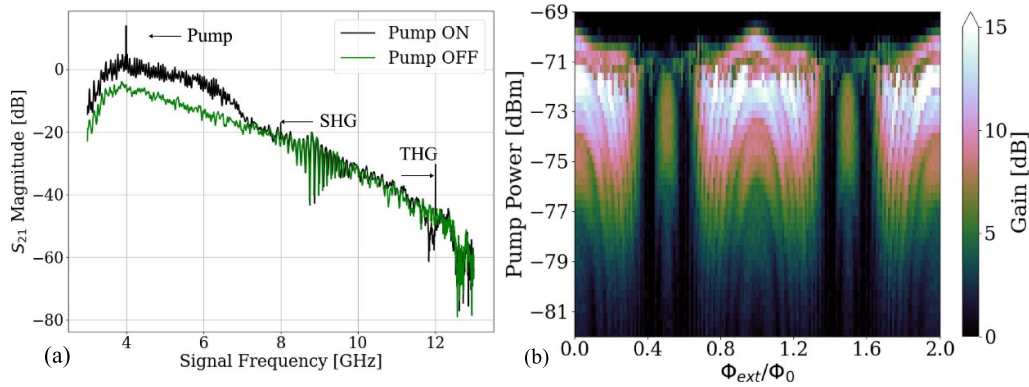
Figure 3. Gain measurements. (a) VNA measurements of the uncalibrated transmission, S_{21} traces, for pump OFF and ON; external magnetic flux $\Phi_{\mathrm{ext}}/\Phi_0 = 0.5$. Pump power at the device is $P_p = -74\,\mathrm{dBm}$. (b) SA gain measurement (difference between pump on and pump off of the power spectral density at the signal frequency) as a function of pump power and external magnetic flux. Pump frequency $f_p = 4\,\mathrm{GHz}$, signal frequency $f_s = 3.9\,\mathrm{GHz}$, signal power at device input $P_s = -110\,\mathrm{dBm}$.
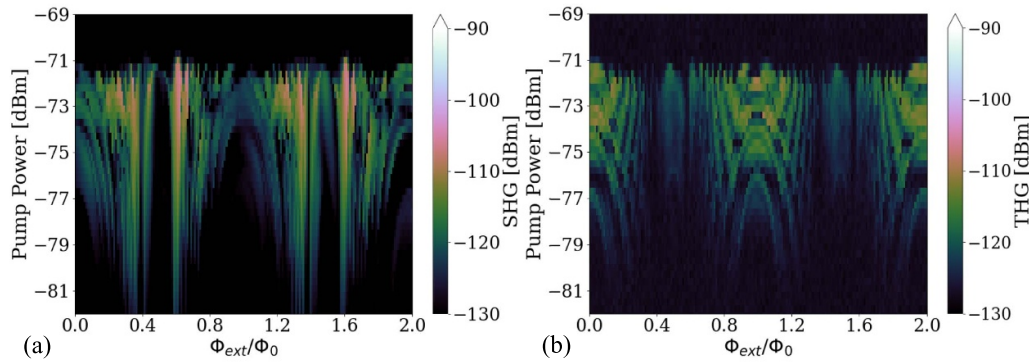
Figure 4. Experimental study of harmonics generation. (a) SHG and (b) THG of the pump measured with a Spectrum Analyzer as a function of pump power and applied flux. Pump frequency $f_p = 4\,\mathrm{GHz}$, signal frequency $f_s = 3.9\,\mathrm{GHz}$, signal power at device input $P_s = -110\,\mathrm{dBm}$.
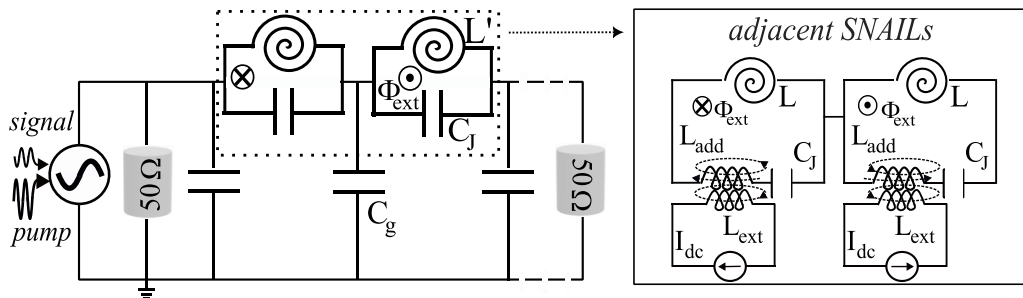
Figure 5. Equivalent circuit of a SNAIL TWPA adopted for numerical simulations in the *WRspice* environment. Here L_{add} is an inductance added to the SNAIL for enabling flux-biasing simulation. C_J is the unit cell Josephson capacitance and L is the inductance per unit cell. C_g indicates the unit cell capacitance to ground. L_{ext} is the inductance of the additional loop. I_{dc} is associated with the WRspice direct current source element. Inversed SNAILs orientation is reproduced by alternating current direction in the DC source.

4. Numerical simulations

To capture the origin of the observed experimental behaviour we perform *WRspice* numerical transient simulations by adopting the equivalent circuit sketched in figure 5 and neglecting losses. To model the flux tunability, we add a small linear inductance, $L_{\mathrm{add}} = 1\,\mathrm{pH}$ in each SNAIL element and consider an auxiliary external inducting loop with inductance $L_{\mathrm{ext}} = 1\,\mathrm{uH}$ [37, 38]. In this way, the flux is coupled via the

external inductance and is controlled by a simulated external source of direct current.

Fabrication-related imperfections among different unit cells are also included in the numerical simulations. Specifically, we introduce a spread in the critical currents of all JJs in the full device (700 cells) by assuming a random Gaussian distribution with mean values equal to the ones estimated from fabrication parameters and linear experimental characterization of the device (see appendix). The
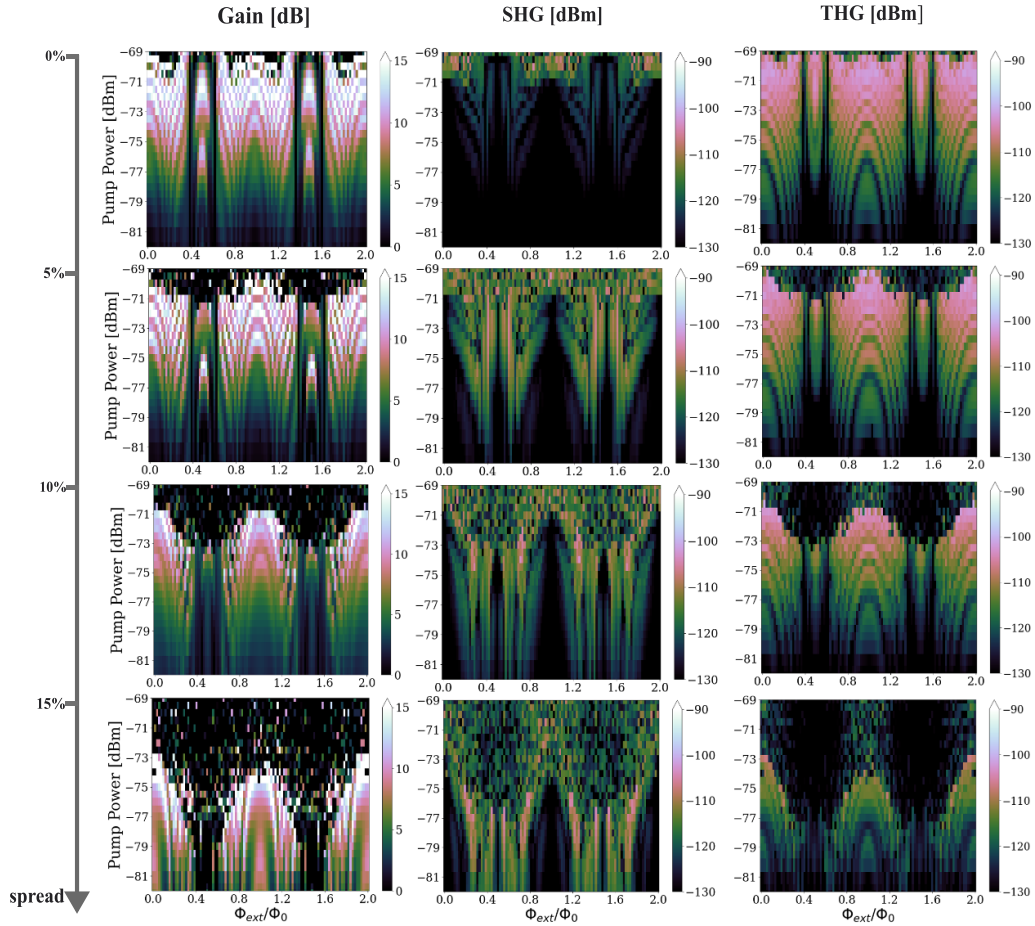
Figure 6. *WRspice* simulation results. The first column is Gain, the second column is SHG and the third column is THG of the pump as a function of pump power and external magnetic flux with different values of JJ critical currents' parameters spread. The spread value changes from $\delta/\langle I \rangle = 0\%$ (top row) up to $\delta/\langle I \rangle = 15\%$ (bottom row). Pump frequency $f_p = 4\,\text{GHz}$, signal frequency $f_s = 3.9\,\text{GHz}$, signal power at device input $P_s = -110\,\text{dBm}$.

standard deviation of the random Gaussian distribution varies from $\delta/\langle I \rangle = 0$ (ideal case in which all junctions with the same designed size have identical critical current) to $\delta/\langle I \rangle = 15\%$ (typical upper limit for JJs' arrays fabrication tolerance [30, 31]).

In figure 6, we show the results of the transient simulations by plotting the signal gain (*pump on—pump off*, differential output spectral power at f_s) and the output spectral power at the pump's harmonics frequencies as a function of pump power and external magnetic flux.

The simulated gain and THG are periodic with the external flux: the observed maxima and minima correspond to the experimentally obtained flux points for all the tested spread values. On the other hand, we find a relevant impact of the JJ's critical current spread on the behaviour of gain and THG as a function of pump power, observing a decrease of the pump saturation power, from roughly $-70\,\text{dBm}$ to roughly $-75\,\text{dBm}$ when the spread amount increases from 0% to 15%. In addition, we also find that the spread in JJ critical currents affects the absolute maximum amplification value, going from about 15 dB for $\delta/\langle I \rangle = 0$–12 dB for $\delta/\langle I \rangle = 15\%$. We interpret the simultaneous reduction of the maximum values for the two

4WM processes, gain and THG, as an effect of the reduced saturation power. By increasing the spread, some of the junctions have a lower critical current, bringing the full device to saturate at lower pump power. Therefore, the maximum achievable gain and THG amplitude is reduced.

Finally, an important outcome following from the numerical simulations is the influence of the spread of JJ's critical currents on the generation of the second harmonic of the pump. While for an ideal device (no spread in the critical current values) SHG of the pump is almost fully suppressed for pump powers below the saturation of the critical current (about $-70\,\text{dB}$), its intensity increases as the spread percentage increases, showing the best qualitative agreement with the flux-dependent experimental behaviour for typical values of fabrication-related JJ's critical current spread of 5%.

We interpret the increase of the SHG with increasing spread in the JJs' critical currents as an effect of the increasing disorder in the alternating flux polarity design. The latter ideally guarantees a full cancellation of the 3WM nonlinearity in the approximation of wavelengths much larger than the unit cells [32]. This is valid because the 3WM coefficient β associated with each SNAIL (see equation (4) in appendix) is an
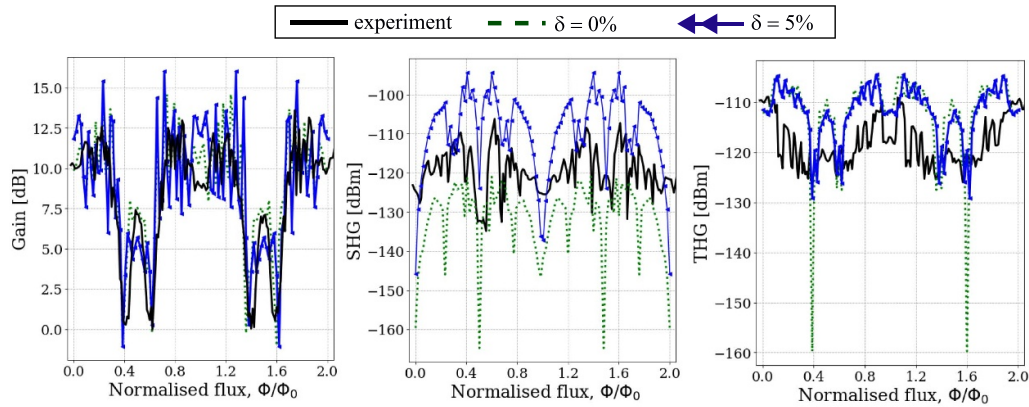
Figure 7. Horizontal cuts of experimentally and numerically obtained 2d-color-maps for -74 dBm pump power. Simulations are reported for the case of 0% and 5% JJs' critical current spread.

odd function of the external flux. In the case of 0 % spread, adjacent SNAILs are identical but with opposite flux polarity. This means that the corresponding β coefficient will have identical absolute value but opposite sign, resulting in an overall suppression of 3WM processes like SHG. By switching on the spread in junction critical currents, adjacent SNAILs and the corresponding β amplitude are not identical anymore, and their difference gets bigger as the spread in junction critical current increases, thus increasing the overall β and so the efficiency of SHG. The residual SHG at 0% spread below the saturation power is attributed to a deviation from the assumption of fully cancelled 3WM nonlinearity for the alternated flux polarity design, corresponding to the approximation of wavelengths much larger than the unit cells [32].

For a more accurate comparison with the experimental results, in figure 7, we report horizontal cuts of both experimentally and numerically obtained 2d-color-maps for a selected pump power of -74 dBm, highlighting the simulations results for 0% and 5% spread. In figure 7, we observe qualitative agreement between experiments and theory for gain and SHG, where the experimental curve lies in between the simulated ones with 0% and 5% spread. However, for the THG case, the simulations are both overestimating the power observed experimentally. We attribute this discrepancy to the fact that our model does not include losses, which in the real device are considerably higher at the frequency of the THG than at the SHG and signal frequencies [7]. The inclusion of losses in the simulations is a promising perspective for future investigations in order to improve the agreement between simulations and experiments at higher frequencies.

5. Conclusion

In conclusion, we presented an experimental and numerical study of harmonics generation in a prototypical JTWPA with SNAIL-based unit cells. Our findings demonstrate the impact of JJs fabrication imperfections on the generation of the pump's harmonics and on gain performance. By reporting for the first time a detailed experimental investigation of the

dominant pump harmonics during the operation of a JTWPA as an amplifier, our work provides new insights for understanding the origin of spurious tones in such devices, fostering the development of both mitigation strategies and potential new exploitation methods of higher order processes in JTWPAs.

Data availability statement

The data that support the findings of this study are openly available at the following URL/DOI: https://doi.org/10.5281/zenodo.11498843.

Appendix A. Experiment setup

The cryogenic part of the experimental setup is shown in figure 8. The total input line attenuation is estimated considering the sum of all the cryogenic attenuators, reaching in total -50 dB, and the nominal attenuation of the input RF cables (-10 dB). The output line includes two circulators in series at the 10 mK stage of the dilution refrigerator and a high electron mobility transistor (HEMT) cryogenic amplifier at the 4 K stage. The HEMT working frequency range is from 4 GHz to 12 GHz with a nominal amplification of about 40 dB. At 300 K, a room-temperature amplifier providing about 30 dB amplification is installed. For flux biasing the TWPA, a superconducting coil is placed alongside the device holder.
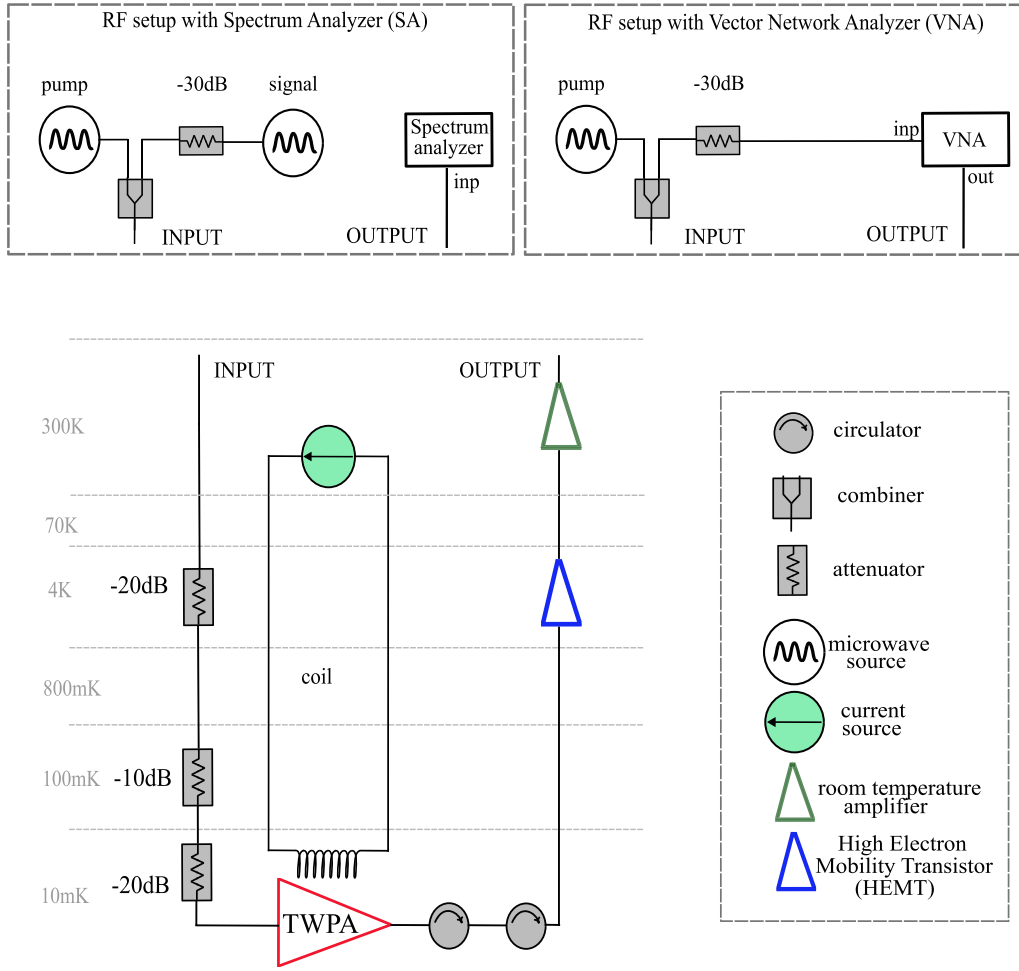
Figure 8. Sketch of the experimental setup. The top insets represent the room-temperature part of the setup showing the two adopted configurations using either the spectrum analyzer or the vector network analyzer. The bottom scheme reports the cryogenic setup inside the dilution refrigerator.

We adopt two main room-temperature setups (figure 8 insets). For transmission measurements like the one reported in figure 3(a), a VNA is used, and its output is combined with the one of an RF source used for pumping the device. For spectral power characterizations like the one reported in figures 3(b) and 4, a SA is used and two different RF sources are combined to send the pump and signal in input.

Appendix B. Characterizations of the device in the linear regime

We perform a preliminary linear measurement of the device under investigation in order to characterize the flux tunability and estimate the critical current I_c and the SNAIL ratio r. Other circuit parameters, such as the ground capacitance C_g, the SNAIL Josephson capacitance C_J, and the number of cells, are obtained from design and fabrication values [7] and reported in table 1.

The linear characterization is performed following the procedure reported in the supplementary information of [7]. In

detail, we sweep the current in the coil and measure S_{21} TWPA transmission (magnitude and phase) as a function of the external magnetic flux using the VNA setup with a low VNA signal power and no pump in input. The periodic modulation of the TWPA transmission with the applied magnetic flux is due to the flux-dependence of the characteristic impedance, $Z = \sqrt{L/C_g}$. By subtracting from the S_{21} phase a 'reference phase' obtained by substituting the TWPA with a 'dummy PCB device', we get the net transmitted phase $\Theta_{\text{TWPA}}(\omega)$, which is related to the dispersion relation as follow $k(\omega) = \Theta_{\text{TWPA}}(\omega)/N$, where N is the number of unit cells. By assuming disperion without mixing, $k(\omega) = N\sqrt{LC_g}\omega/\sqrt{1 - \frac{\omega^2}{LC_J}}$, for each value of the magnetic flux we can extract L (inductance per unit cell). The latter values are reported in figure 9(b) together with the fit function that takes into account the analytic expression for L as a function of the critical current value I_c and the SNAIL ratio r which are used as fitting parameters. From the best fit we estimate $I_c = 2.6\,\mu A$ and $r = 0.08$.

Figure 9(a) reports the device losses as a function of frequency and applied flux.

Table 1. Parameters of the device extracted from design and fabrication values.

| Parameter	Value
Number of cells, N	700
Josephson capacitance, C_J	31 fF
ground capacitance, C_g	250 fF
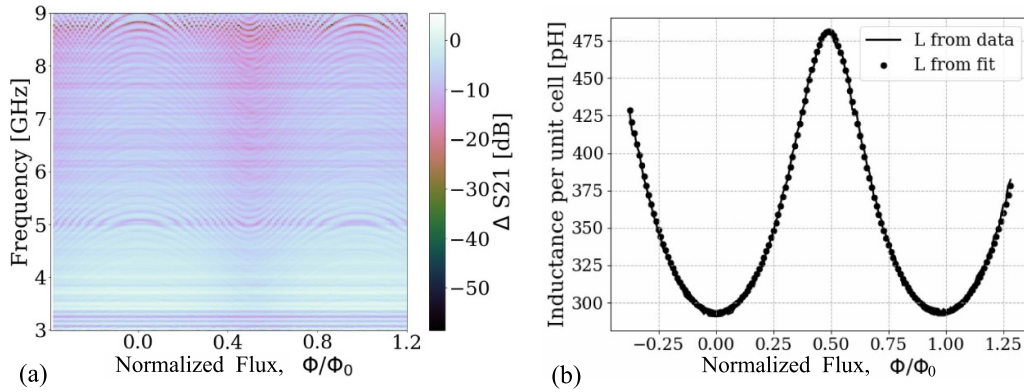
Figure 9. Linear characterisation and parameters extraction. (a) Difference between transmissions of TWPA and 'dummy device'. (b) Experimentally obtained and fitted inductance of unit cell.
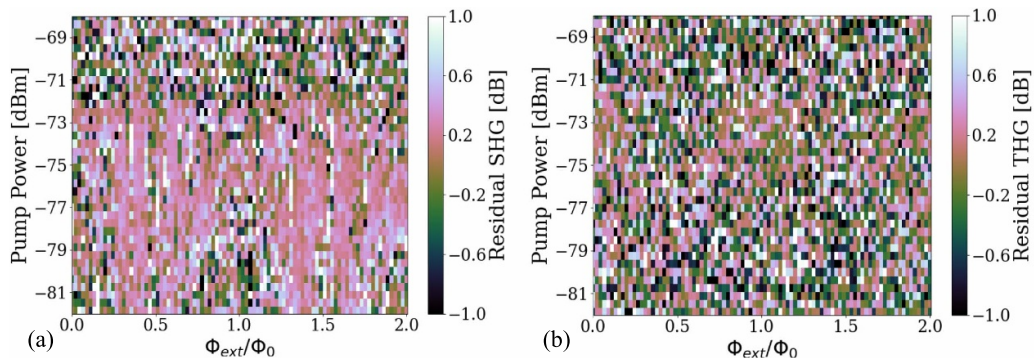
Figure 10. Residual pump harmonics spectral power obtained performing the difference between the case with *input signal on* and *input signal off* for SHG (left) and THG (right). Pump frequency $f_p = 4$ GHz, signal frequency $f_s = 3.9$ GHz, signal power at device input $P_s = -110$ dBm.

Appendix C. Influence of input signal on pump harmonics generation

We provide the measurement results of the SHG and THG with and without the input signal. In figure 10 we plot the experimental residual spectral power for SHG and THG obtained calculating the difference between the case with *input signal on* and with *input signal off*. We observe that the presence of the signal does not significantly influence the pump's harmonics generation (see appendix).

Appendix D. Experiments in a large range of external magnetic flux

In figure 11, we report the experimental results for TWPA SHG and THG in an extended range of external magnetic flux that here we express in terms of the current in the coil. The reported range is the maximum range of current values before starting to observe an increase in the base cryostat temperature. Along with the expected flux-dependent periodicity, we also observe an additional slow modulation with the external flux. (The flux range for the data reported in figures 3 and 4 corresponds to the
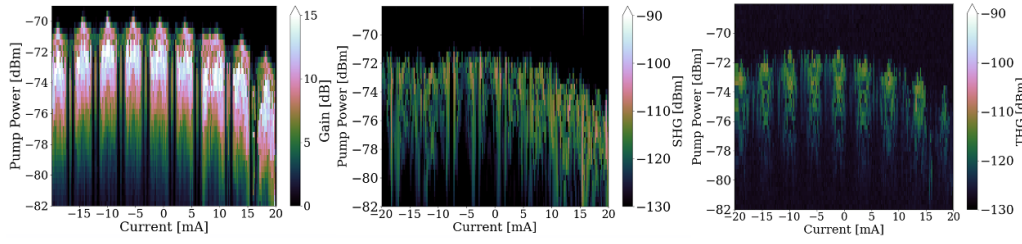
Figure 11. Experimental behaviour in a large range of external magnetic flux. Gain (left), SHG (middle) and THG (right) as a function of pump power and current in the coil placed underneath the sample. Pump frequency $f_p = 4\,$GHz, signal frequency $f_s = 3.9\,$GHz, signal power at device input $P_s = -110\,$dBm.

range between -10 mA and 0 mA, in terms of direct current of the coil.)

The observed slow modulation with the external flux can be explained by the fact that during the experiment no magnetic shielding has been adopted, making the measurements sensitive to additional environmental magnetic fields. Specifically, as recently reported in [39, 40], the JJ critical current can be affected by magnetic field lines along the insulating layer of JJs due to the 'bending' of the total perpendicular magnetic field.

Appendix E. Coupled mode equations theory

Here we report the main derivation steps to obtain the analytical expressions for gain and THG displayed in figure 2, following the standard coupled mode equations approach developed in [2, 24, 33]. First we provide the definition for the main flux dependent parameters. To do so, we start from the Taylor expansion of the current I_L through a SNAIL unit cell:

$$\frac{I_L(\phi^* + \phi)}{I_C} \approx \tilde{\alpha}\phi - \tilde{\beta}(\phi)^2 - \tilde{\gamma}(\phi)^3, \quad (2)$$

where I_c is the Josephson junction critical current, and the expansion is about a flux ϕ^* such that $I_L(\phi^*) = 0$. The coefficient in equation (2) are defined as follows:

$$\tilde{\alpha} = r\cos\phi^* + \frac{1}{3}\cos\left(\frac{\phi^* - \phi_{\text{ext}}}{3}\right), \quad (3)$$

$$\tilde{\beta} = \frac{1}{2}\left[r\sin\phi^* + \frac{1}{9}\sin\left(\frac{\phi^* - \phi_{\text{ext}}}{3}\right)\right], \quad (4)$$

$$\tilde{\gamma} = \frac{1}{6}\left[r\cos\phi^* + \frac{1}{27}\cos\left(\frac{\phi^* - \phi_{\text{ext}}}{3}\right)\right]. \quad (5)$$

Considering the alternating flux polarity design of the device under investigation, we neglect the 3WM nonlinear coefficient, assuming $\tilde{\beta} = 0$ for any value of the external flux. Note

that the coefficients $\tilde{\gamma}$ and $\tilde{\alpha}$ are associated with the g_4 4WM coupling rate via the following relation: $\hbar g_4 = \frac{\tilde{\gamma}}{2\tilde{\alpha}}E_C$, where $E_C = e^2/(2C_g)$ is the charging energy.

Given the definitions above, equation (1) can be rewritten as

$$\frac{\partial^2 \phi}{\partial x^2} - \frac{1}{\omega_0^2}\frac{\partial^2 \phi}{\partial t^2} + \frac{1}{\omega_J^2}\frac{\partial^4 \phi}{\partial x^2 \partial t^2} - \gamma\frac{\partial}{\partial x}\left[\left(\frac{\partial \phi}{\partial x}\right)^3\right] = 0, \quad (6)$$

where $\gamma = \tilde{\gamma}/\tilde{\alpha}$, $L = \Phi_0/(2\pi I_C\tilde{\alpha})$ and Φ_0 being the magnetic flux quantum.

To find the analytical expression for the 4WM gain, the following ansatz is considered [24, 33]:

$$\phi(x,t) = \frac{1}{2}\left[A_p(x)\,e^{i(k_p x - w_p t)} + A_s(x)\,e^{i(k_s x - w_s t)}\right.$$
$$\left. + A_i(x)\,e^{(k_i x - w_i t)} + c.c.\right]. \quad (7)$$

By inserting the ansatz solution in equation (6), one obtains a set of three coupled differential equations describing the propagation of pump, signal and idler tones. Using a number of approximations, such as the slowly varying envelope approximation, the approximation of uniform transmission line, undepleted pump assumption and the assumption of a large pump amplitude relative to signal and idler, the final expression for the power gain is:

$$G_{\text{power}} = \cosh^2(gx) + \frac{\Delta k^2}{4g^2}\sinh^2(gx), \quad (8)$$

where g is the reduced gain coefficient given by

$$g = \sqrt{\left(\frac{k_s^2 k_i^2 (2k_p - k_i)(2k_p - k_s)\omega_p^4}{k_p^6 \omega_s^2 \omega_i^2}\right)\alpha_p^2 - \left(\frac{\Delta k}{2}\right)^2}. \quad (9)$$

The total phase mismatch is defined as $\Delta k = k_s + k_i - 2k_p + 2\alpha_p - \alpha_i - \alpha_s$, where the coefficients α_m $(m = p, s, i)$ are defined as follows:

$$\alpha_p = \frac{3\,\gamma\,\omega_0^2\,k_p^5}{8\,\omega_p^2}|A_p|^2 \quad,\quad \alpha_s = \frac{3\,\gamma\,\omega_0^2\,k_p^2\,k_s^3}{4\,\omega_s^2}|A_p|^2 \quad,$$

$$\alpha_i = \frac{3\,\gamma\,\omega_0^2\,k_p^2\,k_i^3}{4\,\omega_i^2}|A_p|^2, \tag{10}$$

and the wave-vectors for signal, idler and pump can be obtained from the chromatic dispersion relation

$$k = \frac{\omega}{\omega_0\sqrt{1 - \omega^2/\omega_J^2}}. \tag{11}$$

A similar approach can be adopted to obtain the analytical expression for the THG amplitude [24]. In this case, the ansatz solution includes only pump and the third harmonic waves:

$$\phi(x,t) = \frac{1}{2}\left[A_p(x)\,e^{i(k_p x - w_p t)} + A_h(x)\,e^{i(k_h x - w_h t)} + c.c.\right], \tag{12}$$

where $\omega_h = 3\omega_p$. The final expression for THG amplitude is given by:

$$A_h = \kappa_2\frac{1 - e^{ix(\Delta k + 3\kappa_0 - \kappa_1)}}{\Delta k + 3\kappa_0 - \kappa_1}\,e^{-i\kappa_1 x}, \tag{13}$$

with $\Delta k = 3k_p - k_h$ being the chromatic phase mismatch, and the coefficients defined as follows,

$$\kappa_0 = \gamma\frac{3\,k_p^5\,\omega_0^2\,|A_{p0}|^2}{8\,\omega_p^2}, \qquad \kappa_1 = \gamma\frac{6\,k_p^2\,k_h^3\,\omega_0^2\,|A_{p0}|^2}{8\,\omega_p^2},$$

$$\kappa_2 = \gamma\frac{3\,k_p^4\,k_h\,\omega_0^2\,A_{p0}^3}{8\,\omega_p^2}, \tag{14}$$

with $|A_{p0}|$ the pump amplitude at the input of the device.

Appendix F. Frequency-dependent gain profile

In figure 12 we report a comparison between the experimental frequency-dependent gain profile (differential trace of the 'pump ON' and 'pump OFF' traces in figure 3(a)) and simulations for different spread values of the Josephson junctions critical current. For low frequencies, lower than about 4.5 GHz, we observe qualitative agreement between the experimental data and the simulations for typical values of fabrication-related JJ's critical current spread of 5%. This is consistent with the results reported in the main text for a representative signal frequency at 3.9 GHz. The agreement between experiments and $\delta = 5\%$ simulations gets slightly worse for higher frequencies. This could be explained considering the decrease of dielectric losses with increasing power due to the saturation of two-level systems (TLS) in the real device [41, 42]. This effect could lead to an overestimation of the experimental gain for higher frequencies, where losses are higher [7].
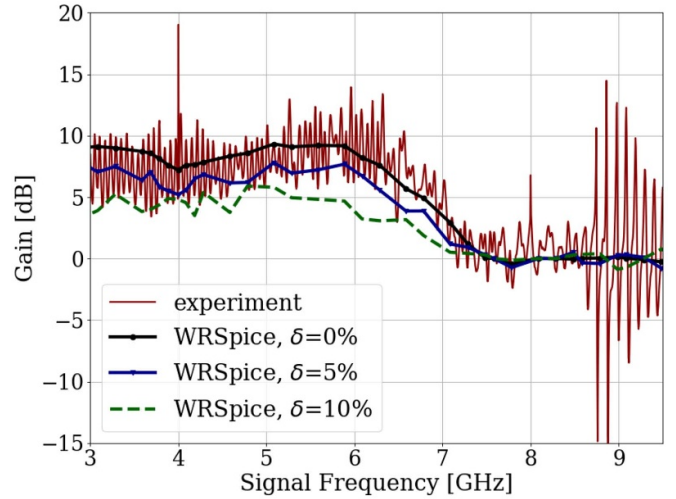
Figure 12. Comparison between the experimental frequency dependent gain profile (differential trace of the 'pump ON' and 'pump OFF' traces reported in figure 3(a)) and WRSpice simulations for spread values $\delta = 0\%$, $\delta = 5\%$ and $\delta = 10\%$. External magnetic flux $\Phi_{\text{ext}}/\Phi_0 = 0.5$. Pump power at the device is $P_p = -74\,\text{dBm}$.
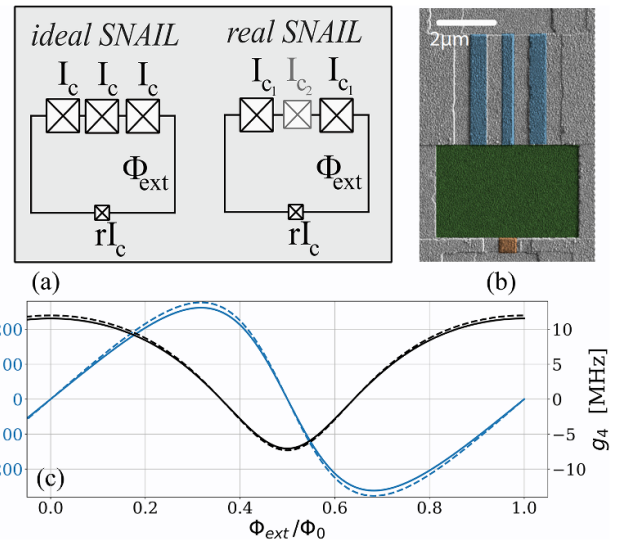
Figure 13. SNAIL fabrication imperfections influence. (a) Sketches of an ideal and a real SNAIL. (b) SEM SNAIL. Reproduced from [7]. CC BY 4.0. (c) 3WM (g_3) and 4WM (g_4) non-linear coefficients as a function of flux for both ideal (continuous lines) and real (dashed lines) SNAIL unit cell.

Appendix G. SNAIL systematic fabrication imperfections influence

In this section we explain in detail how in our simulations we took into account systematic fabrication imperfections associated with the single unit cell. Each SNAIL in the investigated device consists of three large Josephson junctions (with critical currents I_c) and one small junction (with critical current rI_c). The three big JJs are all identical by design (sketch in figure 13(a) left inset), however, the Dolan bridge JJ fabrication method for the SNAIL typically induces a dimension

variation such that the junction located in the middle turns out slightly smaller than the side ones (see sketch in figure 13(a) right inset). Such fabrication imperfection can be appreciated in figure 13(b), which illustrates a scanning electron microscopy (SEM) image, adapted from [7], of a typical SNAIL in the device. In order to investigate the effect of such systematic fab imperfection, from the SEM image we estimated the ratio between the area of the two big top junctions and the area of the smaller middle top junction $a_1/a_2 = 1.3$. In our simulations, we took into account this effect assuming that the average critical current for the three top junctions is given by the value I_c estimated in appendix B.

In addition, for a better comprehension of the effect of such systematic imperfection, we compared the analytical predictions for 3WM and 4WM nonlinear coefficients g_3 and g_4 of an ideal SNAIL and the ones of a real SNAIL (modelled as in the 'real SNAIL' sketch in figure 13(b)—inset) obtained using the recently developed python package 'NINA' (Nonlinear Inductive Network Analyzer) [43], which allows to exactly compute the Taylor expansion coefficients of the effective potential energy function of an arbitrary flux-biased superconducting loop. The result of such comparison is reported in figure 13(c), which shows g_3 and g_4 coefficients as a function of the external magnetic flux for both an ideal (continuous lines) and a real SNAIL (dashed lines). We observe a negligible difference in the two cases and conclude that the aforementioned systematic fabrication imperfection is not significantly affecting the nonlinear processes investigated in this work.

ORCID iDs

A Yu Levochkina ● https://orcid.org/0009-0002-2615-2507
H G Ahmad ● https://orcid.org/0000-0003-2627-2496
I Chatterjee ● https://orcid.org/0009-0007-2249-3378
L Di Palma ● https://orcid.org/0000-0002-7635-5428
R Ferroiuolo ● https://orcid.org/0000-0002-9999-0037
P Darvehi ● https://orcid.org/0000-0001-6567-8574
G Le Gal ● https://orcid.org/0000-0001-6630-0813
D Montemurro ● https://orcid.org/0000-0001-8944-0640
F Tafuri ● https://orcid.org/0000-0003-0784-1454
M Esposito ● https://orcid.org/0000-0002-7674-9195

References

[1] White T C *et al* 2015 Traveling wave parametric amplifier with Josephson junctions using minimal resonator phase matching *Appl. Phys. Lett.* **106** 242601
[2] Bell M T and Samolov A 2015 Traveling-wave parametric amplifier based on a chain of coupled asymmetric squids *Phys. Rev. Appl.* **4** 024014
[3] Macklin C, O'Brien K, Hover D, Schwartz M E, Bolkhovsky V, Zhang X, Oliver W D and Siddiqi I 2015 A near-quantum-limited Josephson traveling-wave parametric amplifier *Science* **350** 307–10
[4] Dietel J Zorin A B, Khabipov M and Dolata R 2018 Traveling-wave parametric amplifier based on three-wave mixing in a Josephson metamaterial *6th Int. Superconductive Electronics Conf. (ISEC)* vol 2018

[5] Miano A and Mukhanov O A 2019 Symmetric traveling wave parametric amplifier *IEEE Trans. Appl. Supercond.* **29** 1–6
[6] Planat L, Ranadive A, Dassonneville R, Puertas Martínez J, Léger S, Naud C, Buisson O, Hasch-Guichard W, Basko D M and Roch N 2020 Photonic-crystal Josephson traveling-wave parametric amplifier *Phys. Rev.* X **10** 021021
[7] Ranadive A, Esposito M, Planat L, Bonet E, Naud C, Buisson O, Guichard W and Roch N 2022 Kerr reversal in Josephson meta-material and traveling wave parametric amplification *Nat. Commun.* **13** 1737
[8] Peng K, Naghiloo M, Wang J, Cunningham G D, Ye Y and O'Brien K P 2022 Floquet-mode traveling-wave parametric amplifiers *PRX Quantum* **3** 020306
[9] Braggio C *et al* 2022 A haloscope amplification chain based on a traveling wave parametric amplifier *Rev. Sci. Instrum.* **93** 094701
[10] Bartram C *et al* 2023 Dark matter axion search using a Josephson traveling wave parametric amplifier *Rev. Sci. Instrum.* **94** 044703
[11] Di Vora R *et al* 2023 Search for galactic axions with a traveling wave parametric amplifier *Phys. Rev.* D **108** 062005
[12] Roudsari A F *et al* 2023 Three-wave mixing traveling-wave parametric amplifier with periodic variation of the circuit parameters *Appl. Phys. Lett.* **122** 052601
[13] Esposito M *et al* 2022 Observation of two-mode squeezing in a traveling wave parametric amplifier *Phys. Rev. Lett.* **128** 153603
[14] Perelshtein M R *et al* 2022 Broadband continuous-variable entanglement generation using a Kerr-free Josephson metamaterial *Phys. Rev. Appl.* **18** 024063
[15] Qiu J Y *et al* 2023 Broadband squeezed microwaves and amplification with a Josephson travelling-wave parametric amplifier *Nat. Phys.* **19** 706–13
[16] Casariego M *et al* 2023 Propagating quantum microwaves: towards applications in communication and sensing *Quantum Sci. Technol.* **8** 023001
[17] Roy A and Devoret M 2016 Introduction to parametric amplification of quantum signals with Josephson circuits *C. R. Phys.* **17** 740–55
[18] Aumentado J 2020 Superconducting parametric amplifiers: the state of the art in Josephson parametric amplifiers *IEEE Microw. Mag.* **21** 45–59
[19] Esposito M, Ranadive A, Planat L and Roch N 2021 Perspective on traveling wave microwave parametric amplifiers *Appl. Phys. Lett.* **119** 120501
[20] Sakuraba I 1963 Extension of traveling-wave parametric amplifier theory *Proc. IEEE* **51** 371–2
[21] McKinstrie C J, Yu M, Raymer M G and Radic S 2005 Quantum noise properties of parametric processes *Opt. Express* **13** 4986–5012
[22] Chaudhuri S, Gao J and Irwin K 2015 Simulation and analysis of superconducting traveling-wave parametric amplifiers *IEEE Trans. Appl. Supercond.* **25** 1–5
[23] Erickson R P and Pappas D P 2017 Theory of multiwave mixing within the superconducting kinetic-inductance traveling-wave amplifier *Phys. Rev.* B **95** 104506
[24] O'Brien K, Macklin C, Siddiqi I and Zhang X 2014 Resonant phase matching of Josephson junction traveling wave parametric amplifiers *Phys. Rev. Lett.* **113** 157001
[25] Dixon T, Dunstan J W, Long G B, Williams J M, Meeson P J and Shelly C D 2020 Capturing complex behavior in Josephson traveling-wave parametric amplifiers *Phys. Rev. Appl.* **14** 034058
[26] Renberg Nilsson H, Fadavi Roudsari A, Shiri D, Delsing P and Shumeiko V 2023 High-gain traveling-wave parametric amplifier based on three-wave mixing *Phys. Rev. Appl.* **19** 044056
[27] Frattini N E, Sivak V V, Lingenfelter A, Shankar S and Devoret M H 2018 Optimizing the nonlinearity and

dissipation of a snail parametric amplifier for dynamic range *Phys. Rev. Appl.* **10** 054020

[28] Katayama H, Hatakenaka N, Fujii T and Blencowe M P 2023 Analog black-white hole solitons in traveling wave parametric amplifiers with superconducting nonlinear asymmetric inductive elements *Phys. Rev. Res.* **5** L022055

[29] Whiteley Research Inc 2024 *WRspice Circuit Simulator* (available at: www.wrcad.com/wrspice.html) (Accessed 2024)

[30] Peatáin S G Ó, Dixon T, Meeson P J, Williams J, Kafanov S and Pashkin Y A 2023 Simulating the effects of fabrication tolerance on the performance of Josephson travelling wave parametric amplifiers *Supercond. Sci. Technol.* **36** 045017

[31] Kissling C, Gaydamachenko V, Kaap F, Khabipov M, Dolata R, Zorin A B and Grünhaupt L 2023 Vulnerability to parameter spread in josephson traveling-wave parametric amplifiers *IEEE Trans. Appl. Supercond.* **33** 1–6

[32] Zorin A B 2021 Quasi-phasematching in a poled Josephson traveling-wave parametric amplifier with three-wave mixing *Appl. Phys. Lett.* **118** 222601

[33] Yaakobi O, Friedland L, Macklin C and Siddiqi I 2013 Parametric amplification in Josephson junction embedded transmission lines *Phys. Rev.* B **87** 144301

[34] Blais A, Arne L G, Girvin S M and Wallraff A 2021 Circuit quantum electrodynamics *Rev. Mod. Phys.* **93** 025005

[35] Levochkina A 2024 *CMETANA (Couple Mode Equation Theory Analyzer)* (http://dx.doi.org/10.5281/zenodo.10670858)

[36] Levochkina A and Esposito M 2024 Raw experimental data: Investigating pump harmonics generation in a SNAIL-based traveling wave parametric amplifier *Zenodo* (https://doi.org/10.5281/zenodo.11498843)

[37] Aggarwal A 2021 Josephson traveling wave parametric amplifier (JTWPA): noise characterization and harmonics generation *Master Thesis* Grenoble University

[38] Levochkina A Y, Ahmad H G, Mastrovito P, Chatterjee I, Massarotti D, Montemurro D, Tafuri F, Pepe G P and Esposito M 2024 Numerical simulations of Josephson traveling wave parametric amplifiers (JTWPAS): comparative study of open-source tools *IEEE Trans. Appl. Supercond.* **34** 1–7

[39] Mukhopadhyay S, Senior J, Saez-Mollejo J, Puglia D, Zemlicka M, Fink J M and Higginbotham A P 2023 Superconductivity from a melted insulator in Josephson junction arrays *Nat. Phys.* **19** 1630–5

[40] Kuzmin R, Mehta N, Grabon N and Manucharyan V E 2023 Tuning the inductance of Josephson junction arrays without SQUIDs *Appl. Phys. Lett.* **123** 182602

[41] Pappas D P, Vissers M R, Wisbey D S, Kline J S and Gao J 2011 Two level system loss in superconducting microwave resonators *IEEE Trans. Appl. Supercond.* **21** 871–4

[42] McRae C R H, Lake R E, Long J L, Bal M, Wu X, Jugdersuren B, Metcalf T H, Liu X and Pappas D P 2020 Dielectric loss extraction for superconducting microwave resonators *Appl. Phys. Lett.* **116** 194003

[43] Miano A, Joshi V R, Liu G, Dai W, Parakh P D, Frunzio L and Devoret M H 2023 Hamiltonian extrema of an arbitrary flux-biased Josephson circuit *PRX Quantum* **4** 030324